et al., 1984; Benevides, et al. 1991). (*e*) The PO_2^- marker near 1092 cm^{-1} is responsive to large changes in the electrostatic environment of the phosphate group (Aubrey et al., 1992; Stangret and Savoie, 1992). (*f*) Various bands in the 1200–1600 cm^{-1} region, assigned to purine and pyrimidine ring vibrations, are sensitive indicators of ring electronic structures and are expected to exhibit perturbations upon metal binding at ring sites. Among the most informative of

molecular-weight DNA. These spectra show that in the presence of alkaline earth metals there is very little change in the Raman spectrum of either high- or low-molecular-weight DNA. However, in the presence of transition metals, the DNA Raman signature is perturbed extensively, and the perturbations are amplified in the case of high-molecular-weight DNA. The most noticeable changes include a decrease in intensity at 834 cm^{-1} and increases in intensity in the interval

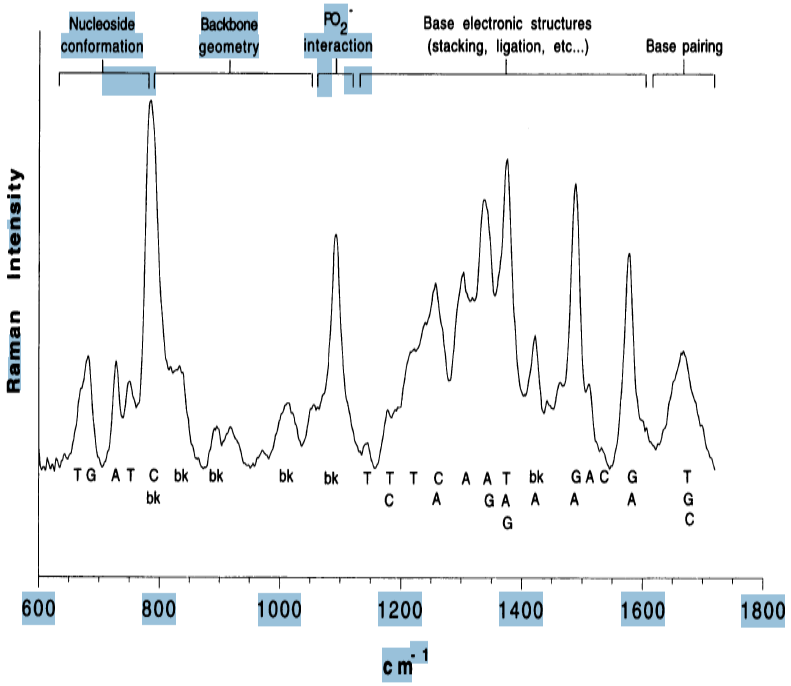

FIGURE 1 Raman spectrum of calf thymus DNA in the region 600–1800 cm^{-1}, showing sensitivity to various conformational features (top labels) and specific vibrational assignments to base (A, T, G, C) and backbone (bk) residues (bottom labels).

Ca^{++} produce significant spectral differences throughout the denaturation of B-form secondary structure. For the present

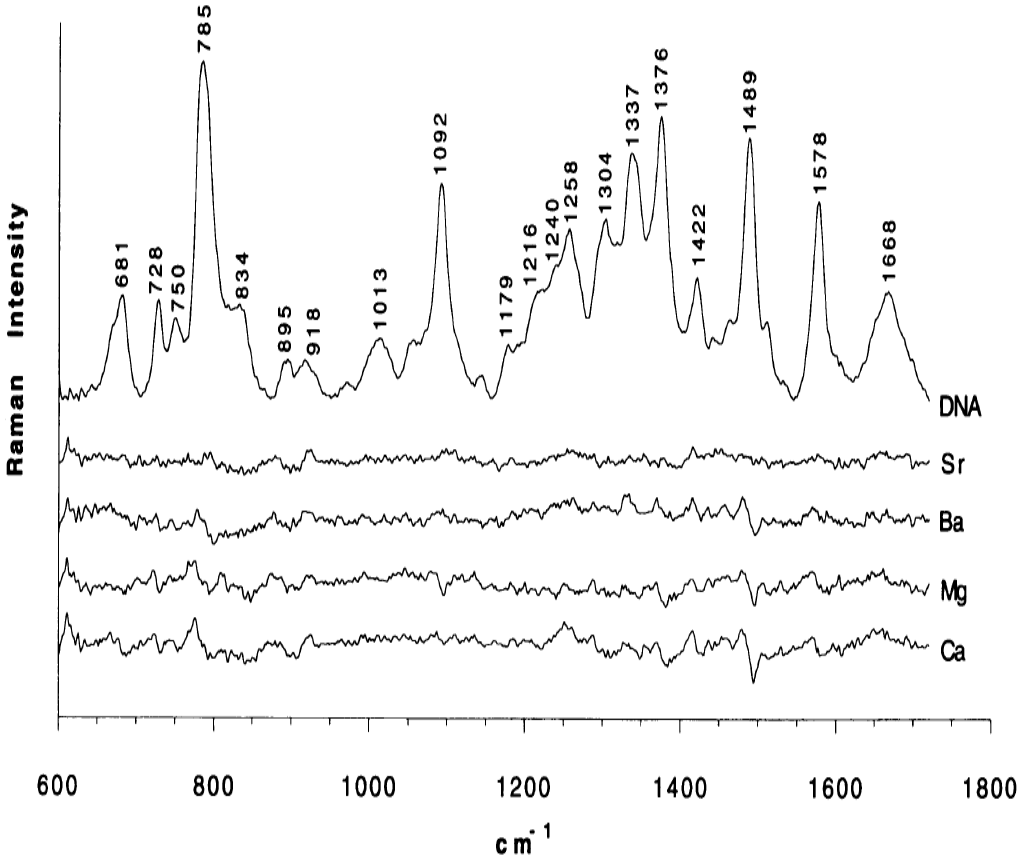

FIGURE 3 From top to bottom: Raman spectrum of 160 bp calf thymus DNA and the difference spectra obtained by its subtraction from spectra of the same DNA in the presence of the indicated alkaline earth metals. Other sample conditions are given in Fig. 1.

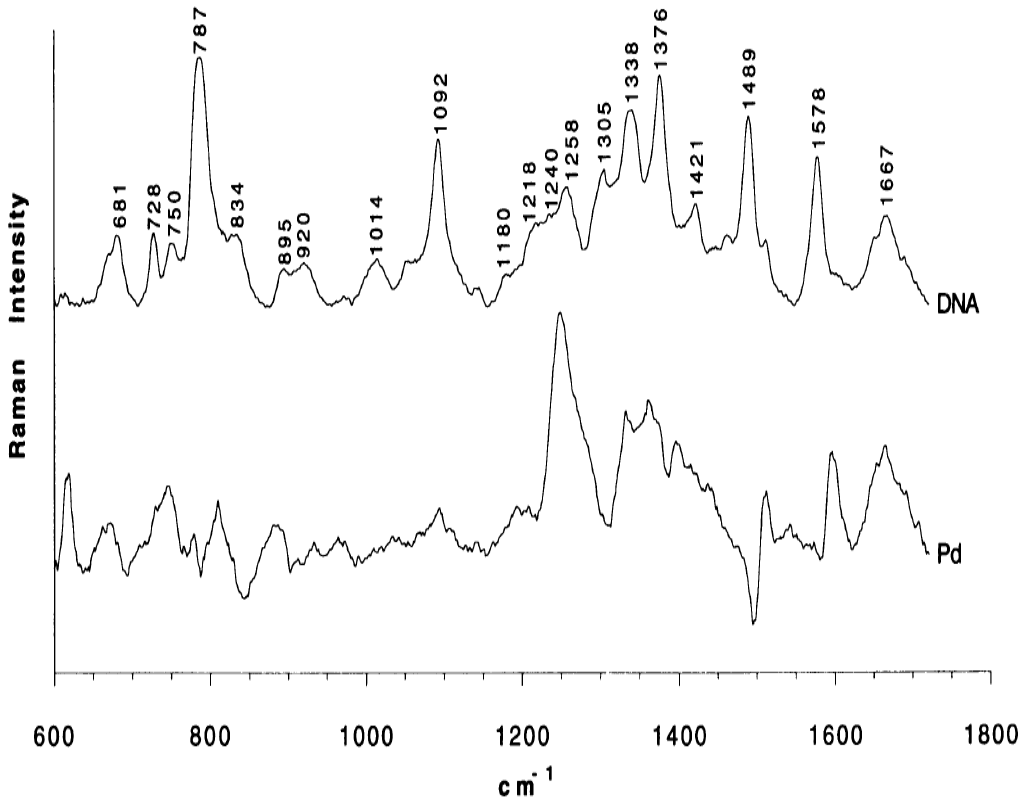

FIGURE 8 Raman spectrum of >23 kbp DNA (*top*) and the difference spectrum obtained by its subtraction from the spectrum of the same DNA in the presence of $PdCl_2$. Sample conditions include 55 mg DNA/ml, 100 mM $PdCl_2$ and 5 mM sodium cacodylate and a temperature of 11°C. Solution pH = 1.7.

ever, relatively little structural information is currently available. X-ray crystallographic studies of complexes between small oligonucleotides and intercalative drugs show that intercalation causes base pair separation of approximately 3.4 Å, as well as helix unwinding that depends upon the identity of the intercalant.[15] Thus, the insertion of the phenanthridinium ring of ethidium bromide (EtBr) into a *B* DNA fragment unwinds the duplex by 26°, reducing the twist angle per base pair from 36° to 10°, whereas insertion of either proflavine (PF) or 9-aminoacridine (9AA) unwinds DNA by about 17° (Fig. 1).[16–18] No structural details are available for solution complexes of EtBr, PF and 9AA with larger DNA targets.[9–11,19]

of DNA and its biological assemblies. In applications to complexes of DNA with highly chromophoric intercalants, near-infrared (NIR) laser wavelengths provide the excitation of choice in order to circumvent the intense absorption and fluorescence interferences encountered with visible wavelength excitations. NIR Raman studies of drug/DNA complexes are expected to reveal structural perturbations of both the *B* DNA target and the intercalating drug, thus providing an important advantage over the complementary but more limited techniques of surface enhanced Raman spectroscopy (SERS) and ultraviolet-resonance Raman (UVRR) spectroscopy.[19,21–23] This has been demonstrated for EtBr/DNA complexes in both solution[10] and crystalline states.[11] Additionally, the NIR Raman probe

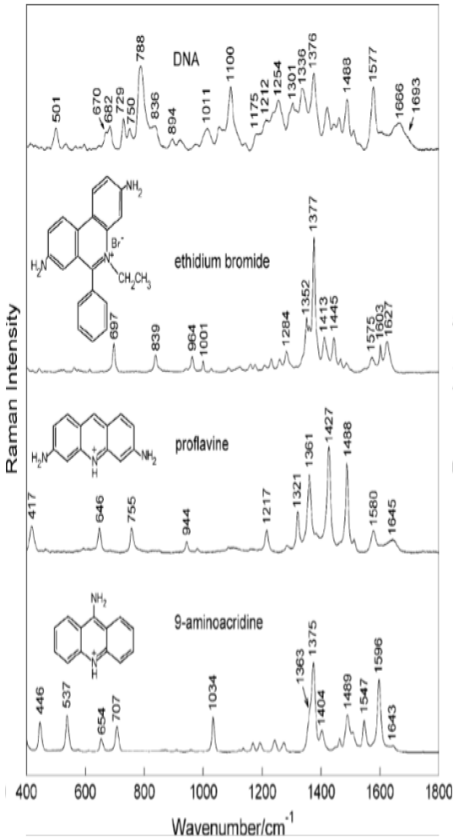

Figure 1. Raman spectra (400–1800 cm^{-1}; 752-nm excitation) of aqueous solutions of calf thymus DNA (25 mg/mL) and the drugs ethidium bromide (1.6 mg/mL), proflavine (3.8 mg/mL) and 9-aminoacridine (5.0 mg/mL), as labeled from top-to-bottom. All

J. Raman Spectrosc. 2008; **39**: 1627–1634
DOI: 10.1002/jrs

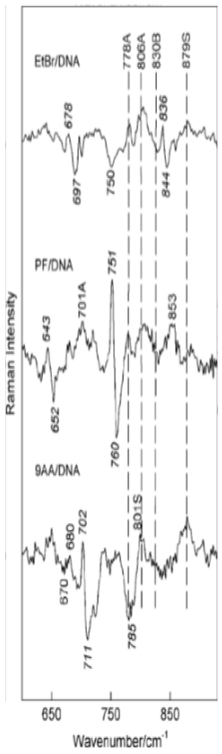

Figure 5. From top-to-bottom: Amplifications of spectral difference profiles (600–900 cm^{-1}) of EtBr/DNA, PF/DNA and 9AA/DNA complexes from Figures 2–4, respectively. Raman markers diagnostic of DNA (see text) are connected by vertical dashed lines and are labeled to indicate their wavenumber values and assignments to either A-form (A), B-form (B) or single-stranded (S) DNA. Italicized labels indicate wavenumber values of Raman markers of the drugs.

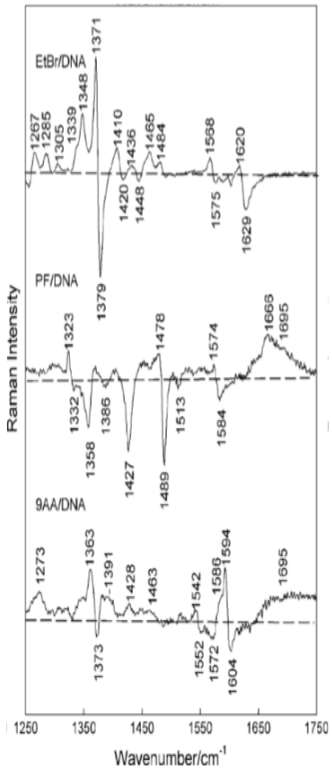

Figure 6. From top-to-bottom: Amplifications of spectral difference profiles (1250–1750 cm^{-1}) of EtBr/DNA, PF/DNA and 9AA/DNA complexes from Figures 2–4, respectively. Raman markers are labeled to indicate wavenumber values and assignments to either the DNA or drug (italics) component of the complex. The ordinate amplification is arbitrary.

consistent with binding of PF to both AT and GC pairs, i.e. PF

distinctive patterns of the difference peaks in PF/DNA (middle trace) and 9AA/DNA (bottom trace) complexes. Thus, PF binding produces a broad peak centered near 1666 cm^{-1} with a shoulder at approximately 1695 cm^{-1}. On the basis of previous studies, the 1666 cm^{-1} band is assignable to dT and the higher wavenumber shoulder to dG. These results are

Perturbations of the Raman spectra and structures of intercalating drugs

Intercalation of each drug examined in this study introduces a characteristic pattern of wavenumber shifts and intensity changes in Raman markers of the drug (Figs 2–4). These

J. Raman Spectrosc. 2008; **39**: 1627–1634
DOI: 10.1002/jrs

spectral perturbations serve as distinctive fingerprints of the respective drug interaction with *B* DNA.

For the case of EtBr/DNA the major effects are wavenumber shifts in the EtBr markers centered at 1371 and 1627 cm^{-1} (Fig. 1). These wavenumber shifts lead to characteristic spectral difference patterns (peak/trough couplets) at 1371/1379 and 1620/1629 cm^{-1}, as seen in Fig. 2. The couplets represent a fingerprint of phenanthridinium intercalation. As shown previously, these spectral perturbations are independent of the base composition of the DNA target.[10]

Similarly, intercalation of 9AA results in characteristic wavenumber shifts (Fig. 4) for Raman markers of the drug. The peak/trough difference couplets at 1363/1373 and 1594/1604 cm^{-1} thus constitute the Raman fingerprint of 9AA intercalation.

For PF/DNA, the difference spectrum (Fig. 3) is dominated by troughs at 1358, 1427 and 1489 cm^{-1} in addition to prominent couplets at 752/762 and 1574/1584 cm^{-1}. The observed troughs indicate that the parent PF marker bands at 1361, 1427 and 1488 cm^{-1} (Fig. 1) suffer large intensity decreases (Raman hypochromism) with intercalation into *B* DNA. Interestingly, comparable hypochromic effects are not observed for any band of either EtBr or 9AA upon intercalation. A possible explanation for these findings is that intercalation of the PF polycyclic ring moiety into DNA – in contrast to intercalations of EtBr and 9AA – reflects a radical change in ring environment vis-à-vis the drug in the absence of DNA. For example, if EtBr and 9AA are extensively self-stacked in the absence of DNA, but PF is not, large Raman hypochromic effects would be expected only for intercalation of PF. Although all three drugs are known to form stable dimers in solution,[40] their relative stacking tendencies are not known. Our results would be consistent with greater self-stacking (in the absence of DNA) by dimers of EtBr and 9AA than by dimers of PF.[21] In this scenario, we assume that

Table 1. Raman markers of drug/DNA intercalations

Complex	DNA difference bands[a]	DNA structural correlation[b]
EtBr/DNA	830 → 806	*B*-form to *A*-form backbone (OPO torsion)
	750 ↓	C2′-*endo*/*anti* dT to C3′-*endo*/*anti* dT
9AA/DNA	830 → 879	*B*-form to ssDNA backbone (OPO torsion)
	785 → 801	*B*-form to ssDNA backbone (OPO torsion)
	~1695 ↑	Altered H-bonding of dG (C=O)
PF/DNA	830 → 853	Modified *B*-form backbone (COPOC torsions)
	830 → 879	*B*-form to ssDNA backbone (OPO torsion)
	1666 ↑	Altered H-bonding of dT (C=O)
	~1695 ↑	Altered H-bonding of dG (C=O)

[a] From Raman difference spectra of Figs 5 and 6. Horizontal arrow indicates shift in the parent Raman band peak with drug intercalation; vertical arrow indicates direction of parent band intensity change with drug intercalation.

[b] Proposed DNA structural change associated with drug intercalation. Nucleotide residues or affected atomic groups are indicated in parentheses.

single-stranded DNA and could be responsible for acridine-induced frameshift mutagenesis.[41,43] As noted above, the key perturbations to Raman markers of the DNA backbone (600–900 cm^{-1} interval) that occur with 9AA intercalation are consistent with the introduction of single-stranded faults (looping-out) in the double helix. Also, perturbations to Raman markers of DNA bases (1600–1700 cm^{-1} interval)

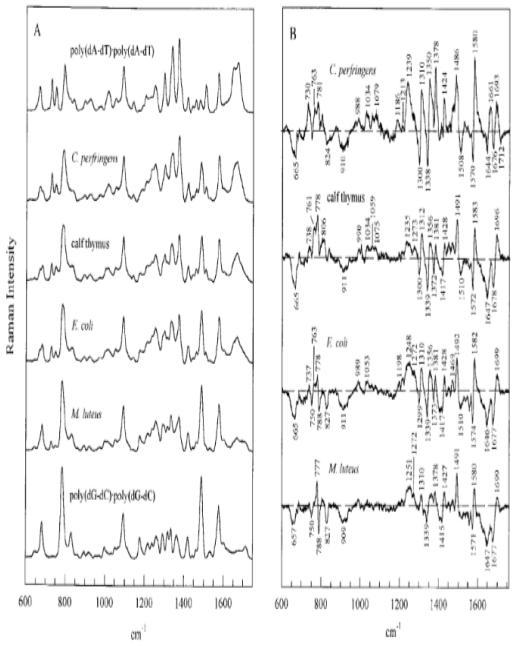

FIGURE 3 Panel A, from top-to-bottom: Raman spectra in the region 600–1750 cm^{-1} of poly(dA-dT)·poly(dA-dT) (0% G + C), *C. perfringens* DNA (27% G + C), calf thymus DNA (42% G + C), *E. coli* DNA (50% G + C), *M. luteus* DNA (72% G + C) and poly(dG-dC)·poly(dG-dC) (100% G + C). Other conditions are as given in Figure 1. Panel B: Difference profile between the observed Raman spectrum of each of the labeled genomic DNAs (minuend) and the weighted spectral sum of poly(dA-dT)·poly(dA-dT) and poly(dG-dC)·poly(dG-dC) of the corresponding base composition (subtrahend). Each difference profile is amplified fourfold compared to the spectrum of the minuend shown in panel A.

virtually identical contributions from guanine and adenine, with respect to both wavenumber value and intensity. The cytosine ring is responsible for the band at 1531 cm^{-1}.

Carbonyl Stretching Modes of dT, dG, and dC. The carbonyl group stretching vibrations of thymine (C2═O and C4═O), guanine (C6═O), and cytosine (C2═O) are expected to give strong Raman bands in

Other Bands of Interest. Raman bands at 895 ± 1, 922 ± 1, 1053 ± 2, 1444 ± 2, and 1462 ± 1 cm^{-1} (Figures 1 and 2), all of which are of weak-to-moderate intensity, are confidently assigned to the deoxyribose moiety. Further discussion of these bands has been given elsewhere.[13,27,37]

The sugar residues of DNA are also expected to be major contributors to the many weak Raman bands observed in the interval 950–1050 cm^{-1} (Figure 1)

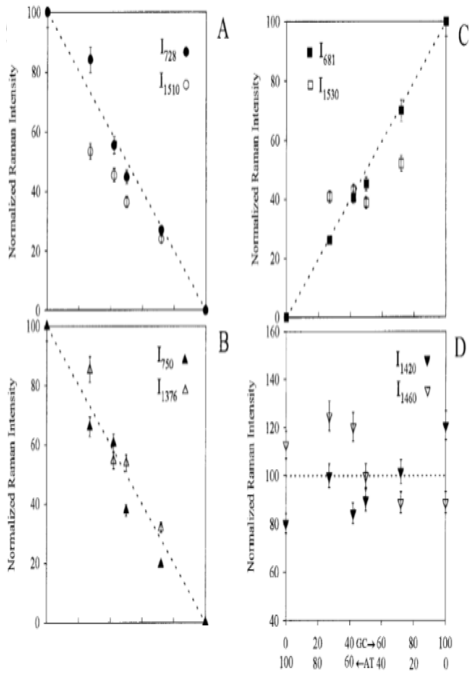

FIGURE 5 Intensities of selected Raman bands of genomic DNA as a function of base composition. Bands of dA (Panel A, 728 and 1510 cm^{-1}) and dT (Panel B, 750 and 1376 cm^{-1}) are normalized to the intensity scale (dashed line) defined by 100% for poly(dA-dT)poly(dA-dT) and 0% for poly(dG-dC)poly(dG-dC). Bands of dG and dC (Panel C, 681 and 1530 cm^{-1}) are normalized to the intensity scale (dashed line) defined by 0% for poly(dA-dT)poly(dA-dT) and 100% for poly(dG-dC)poly(dG-dC). Bands of the deoxyribose-phosphate backbone (Panel D, 1420 and 1460 cm^{-1}) are normalized to the intensity scale (dashed line, 100%) that is independent of base composition. Error bars indicate estimated uncertainties in the spectral intensities, as measured from data of Figures 1–3 and additional spectra (not shown).

(dA, dT, dG, or dC) is *not* influenced by the genomic DNA base sequence but depends only upon base

and 1376 cm^{-1}, Fig. 5B), dG (681 cm^{-1}, Fig. 5C), dC (1530 cm^{-1}, Fig. 5C), and deoxyribose (1420 and

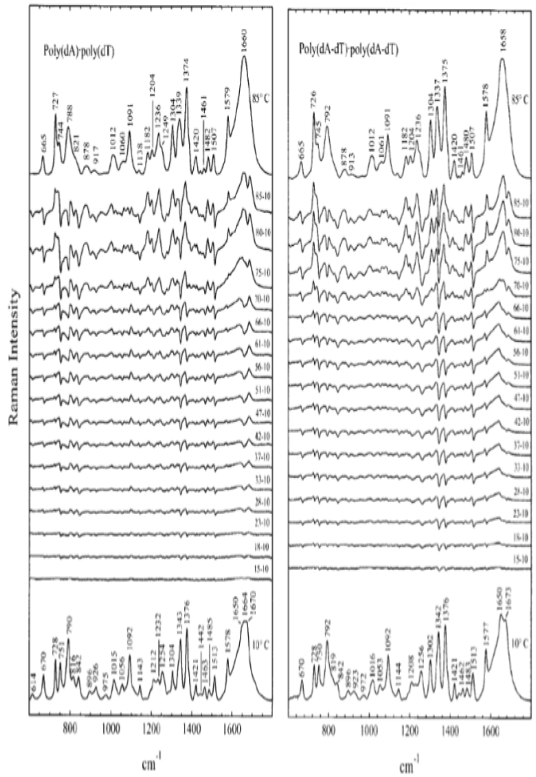

FIGURE 1 Left panel: Raman spectra of poly(dA)·poly(dT) in 100 mM NaCl solution, pH 7.0, at 10°C (bottom trace) and 85°C (top trace). Intermediate traces show the difference spectra computed with the higher temperature spectrum as minuend and the 10°C spectrum as subtrahend. Right panel: Corresponding Raman spectra of poly(dA-dT)·poly(dA-dT) at the same conditions given in the left panel. DNA concentration is 35 mg/mL in each case.

Corresponding data for double-helical poly(dA-dT)· Raman band between the lowest (either 10 or 15°C)

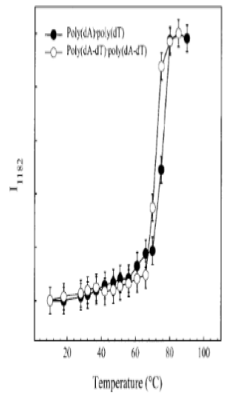

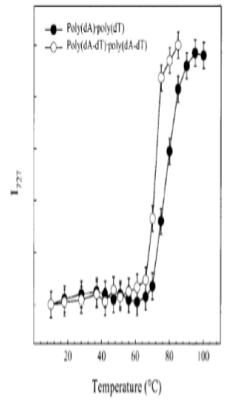

FIGURE 2 Top panel: Temperature dependence of the normalized Raman intensity at 1182 cm^{-1} (I_{1182}) in poly(dA)·poly(dT) (●) and (dA-dT)·poly(dA-dT) (○) over the range $10 < t < 85°C$. The increasing amplitude of I_{1182} with temperature is a quantitative measure of the extent of thymine unpairing and indicates a median melting temperature $T_m = 76.5 \pm 0.4°C$ for poly(dA)·poly(dT). Bottom panel: Temperature dependence of the normalized Raman intensity at 727 cm^{-1} (I_{727}) in poly(dA)·poly(dT) (●) and poly(dA-dT)·poly(dA-dT) (○) over the range $10 < t < 85°C$. The increasing amplitude of I_{727} with temperature

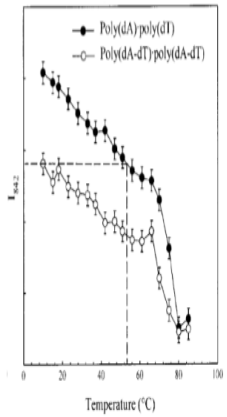

FIGURE 3 Temperature dependence of the normalized Raman intensity at 842 cm^{-1} (I_{842}) in poly(dA)·poly(dT) (●) and poly(dA-dT)·poly(dA-dT) (○) over the range $10 < t < 85°C$. The amplitude of I_{842} is a quantitative measure of ordered phosphodiester C5′–O5′–P–O3′–C3′ linkages in each DNA. The data show that the ordered backbone conformation of poly(dA)·poly(dT) is significantly more thermostable than that of poly(dA-dT)·poly(dA-dT) at all temperatures below complete melting (80°C). For example, the value of I_{842} for poly(dA-dT)·poly(dA-dT) at 10°C is comparable to that of poly(dA)·poly(dT) at 53°C (dashed horizontal line); also at 53°C, poly(dA-dT)·poly(dA-dT) maintains only about one-third of the backbone order of poly(dA)·poly(dT) (dashed vertical line).

Raman Signatures of Premelting and Melting Transitions of Poly(dA)·Poly(dT)

The top panel of Figure 5 compares Raman *difference* signatures for the melting (top trace) and premelting (bottom trace) transitions of poly(dA)·poly(dT). The two are strikingly dissimilar, indicating that very different types of structural changes take place during premelting and melting phases. A corresponding comparison for poly(dA-dT)·poly(dA-dT) is shown in the bottom panel of Figure 5, again demonstrating distinctively different structural changes for the premelting and melting transitions of this structure.

Figure 5 also shows that poly(dA)·poly(dT) and poly(dA-dT)·poly(dA-dT) exhibit dissimilar premelting signatures, particularly with respect to the ampli-

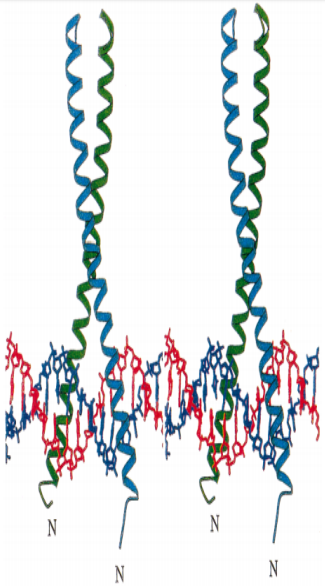

B. λ repressor (HTH)

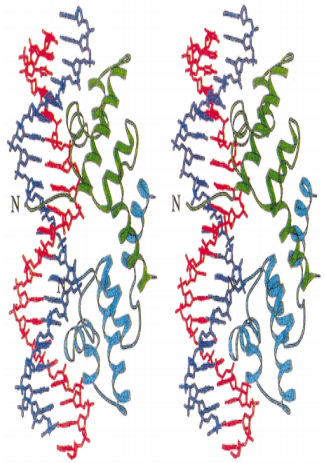

FIGURE 1: (A) Stereo image of the crystal structure of the complex formed between the coiled-coil leucine zipper (bZIP) domain of the yeast transcriptional activator GCN4 and its AP-1-binding site. (B) Stereo image of the crystal structure of the complex formed between

melting (fraying) between 0 and 30 °C.

upon previous studies of B-DNA and have been discussed in detail (*32*, *33*). Diminished hypochromism at 30 °C, due to partial unstacking of bases at the ends of the duplex, accounts for difference peaks at 668 (G, T), 725 (A), 779 (C), 1330 (A, G), 1368 (G), 1483 (G, A), and 1572 (A, G) cm^{-1} (*33*−*35*). Nevertheless, Raman markers of the deoxyribose-phosphate moieties (800−900 cm^{-1}) are not altered appreciably between 0 and 30 °C, indicating that B-form

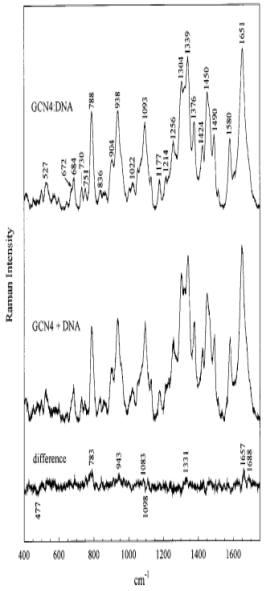

FIGURE 6: Raman spectrum of the specific GCN4:DNA complex (top trace) and the spectral sum of constituents (middle trace), obtained from samples at 0 °C. The difference spectrum (bottom trace) reveals only small spectral perturbations attendant with complex formation.

backbone geometry is largely retained up to 30 °C. ^1H NMR studies of this DNA site (data not shown) lead to the same conclusion.

3. Raman Spectroscopy of the Complex between GCN4 and AP-1. (a) Overview. The Raman spectrum of the specific

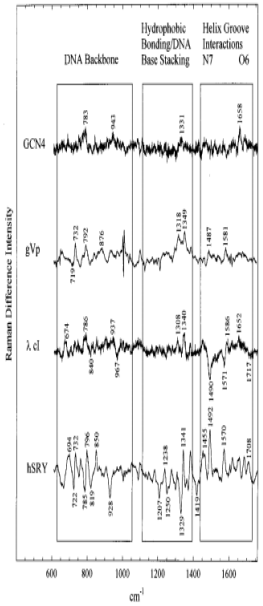

FIGURE 7: Raman difference spectra reflecting DNA reorganizations due to different DNA-binding proteins. From top to bottom: bZIP protein GCN4 binding to an AP-1 target site; ssDNA-binding protein of M13 phage (gVp) binding to the ssDNA analogue, poly-(dA); cI repressor of phage λ binding to its O_L1 target site; human sex determining factor hSRY−HMG box binding to its DNA target site. The Raman signature is minimally perturbed in the unbent GCN4:DNA complex and maximally perturbed in the sharply bent hSRY−HMG:DNA complex (*20*). Ordinates of the difference spectra have been scaled to reflect the same 1090 cm^{-1} intensity in the parent complex. Labeling of boxed segments refers to bands

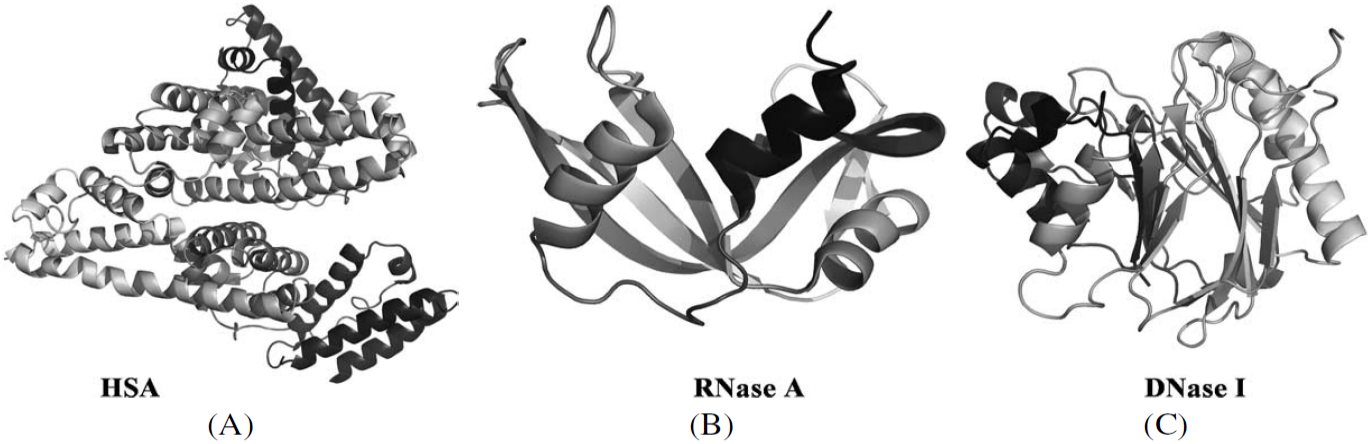

Fig. 1. Ribbon structure of human serum albumin (HSA) (A), RNase A (B), and DNase I (C) derived from their crystal structure determined by X-ray diffraction at 2.5 Å [17], 2.32 Å [58] and 2.8 Å [59], respectively.

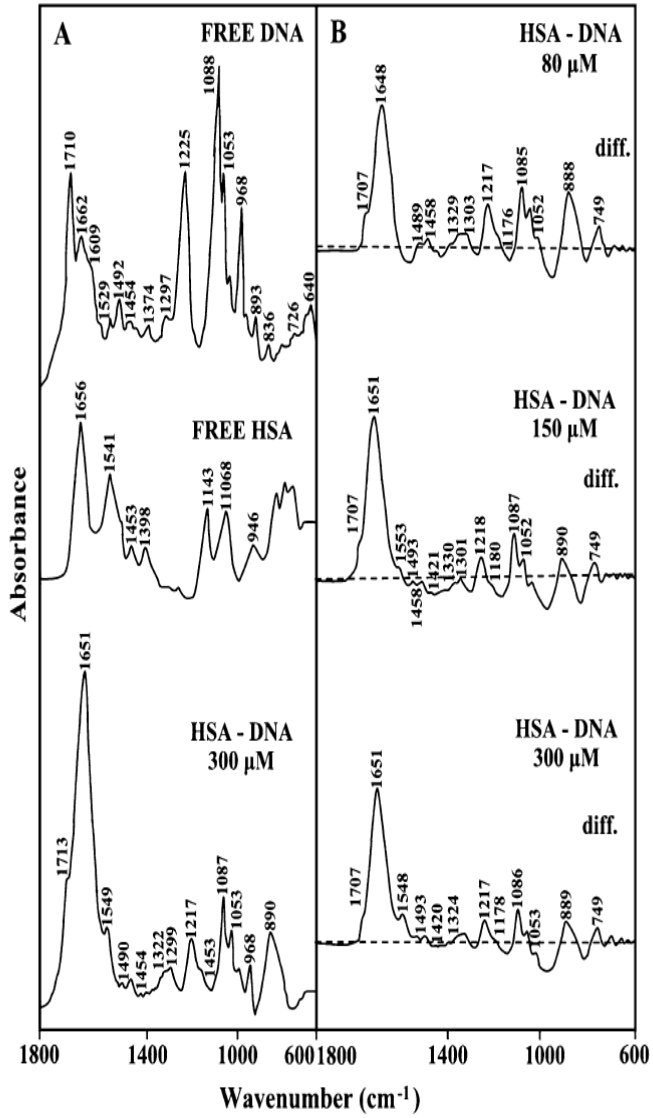

Fig. 2. FTIR spectra (A) and difference spectra [(DNA solution + protein solution) − (DNA solution)] (B) in the region of 1800–1500 cm^{-1} for the free DNA and human serum albumin (HSA) and their complexes in aqueous solution at physiological pH with various protein concentrations.

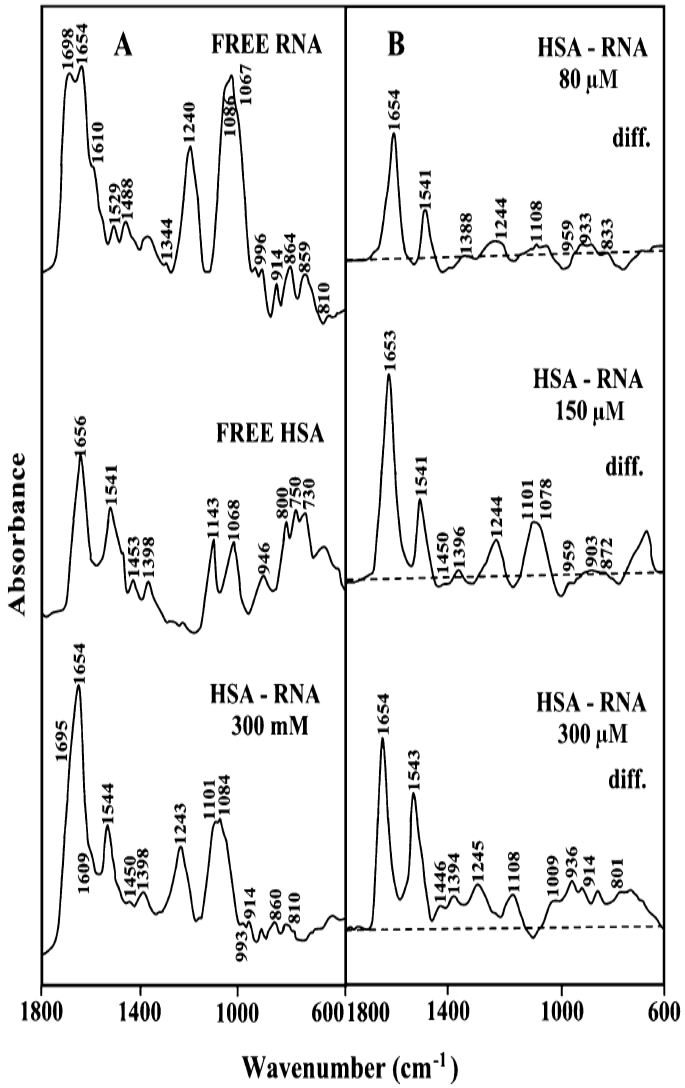

Fig. 3. FTIR spectra (A) and difference spectra [(tRNA solution + protein solution) − (tRNA solution)] (B) in the region of 1800–1500 cm^{-1} for the free tRNA and human serum albumin (HSA) and their complexes in aqueous solution at physiological pH with various protein concentrations.

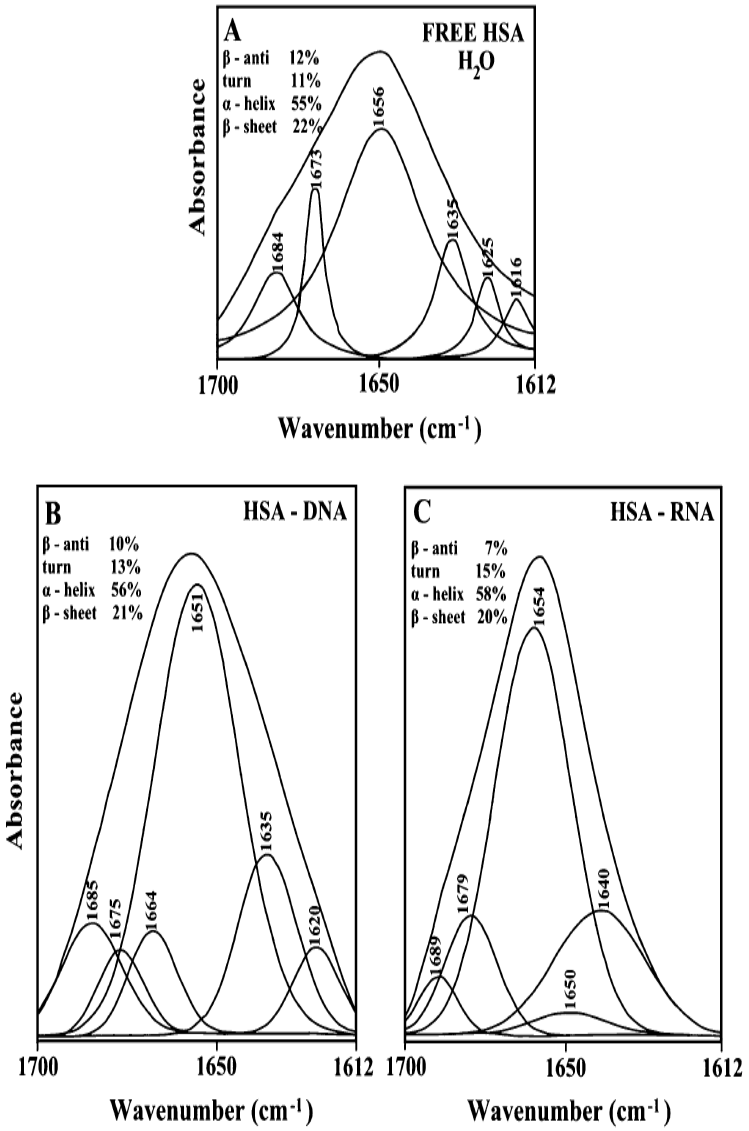

Fig. 4. Curve-fitted amide I region (1700–1612 cm^{-1}) and secondary structure determination of the free human serum albumin (A) and its HSA–DNA (B), and HSA–tRNA (C) in aqueous solution with 300 μM protein and 12.5 mM polynucleotide concentrations.

Surface Enhanced (Resonance) Raman Spectroscopy SE(R)RS v biofyzice

Doc. RNDr. Oldřich Vrána, CSc.

Historie

- 1928 – C.V. Raman, K.S. Krishnan (experiment)
- 1929 – Nobelova cena
- 1970 – RS biopolymerů (DNA, Proteiny)
- 1974 – Fleischman, Hedra and McQuilan (objev SERS efektu)
- 1977 – Jeanmarie, Duyne, resp. Albrecht, Creighton („vysvětlení“ SERS)


SERS Publications
600
500
400
300
200
100
0
1980
1982
1984
1986
1988
1990
1992
1994
1996
1998
2000
2002
2004
2006
Year of publication

Teorie SERS

- SERS je spektroskopická technika, která kombinuje moderni laserovou spektroskopii s vyjímečnými optickými vlastnostmi kovových nanostruktur, což má za následek mnohonásobné zvýšení Ramanova signálu u látek, které se nalézají na nebo v bezprostřední blízkosti povrchu.

Elektromagnetická teorie

k rozptylu dochází v oblasti lokálně zvýšených optických polí (plazmony) na povrchu kovových struktur.

Chemická teorie

molekuly v přímém kontaktu s kovovými nanostrukturami vytvářejí specifické struktury „ nový Ramanovský proces“ se zesílením, které je větší než je tomu u volných molekul (effekt první vrstvy)

SERS aktivní povrchy

Materiály: Ag, Au, Cu ,.....

- ✖ **elektrody**
- ✖ **povrchy s předem upravenou morfologií na něž jsou naneseny výše uvedené kovy**
- ✖ **koloidní částice připravené redukcí Ag/Au solí**
- ✖ **částice o vhodné velikosti pokryté SERS aktivním kovem**

Výhody SERS:

- ✖ citlivost ve srovnání s RS vyšší o 3-5 řádů
- ✖ v případě rezonančního efektu o další cca 4 řády
- ✖ efektivní zhášení fluorescence
- ✖ různé typy povrchů
- ✖ spojení s dalšími metodami (elektrochemie, AFM)

Omezení SERS:

- krátký dosah (biomakromolekuly)
- závislost spektra na orientaci molekuly
- interakce s povrchem může vyvolávat denaturaci (artefakty)
- „kontaminace“ spekter
- omezená stabilita koloidů, nutnost aktivace

UV-VIS spektra roztoku koloidních částic v závislosti na stupni agregace

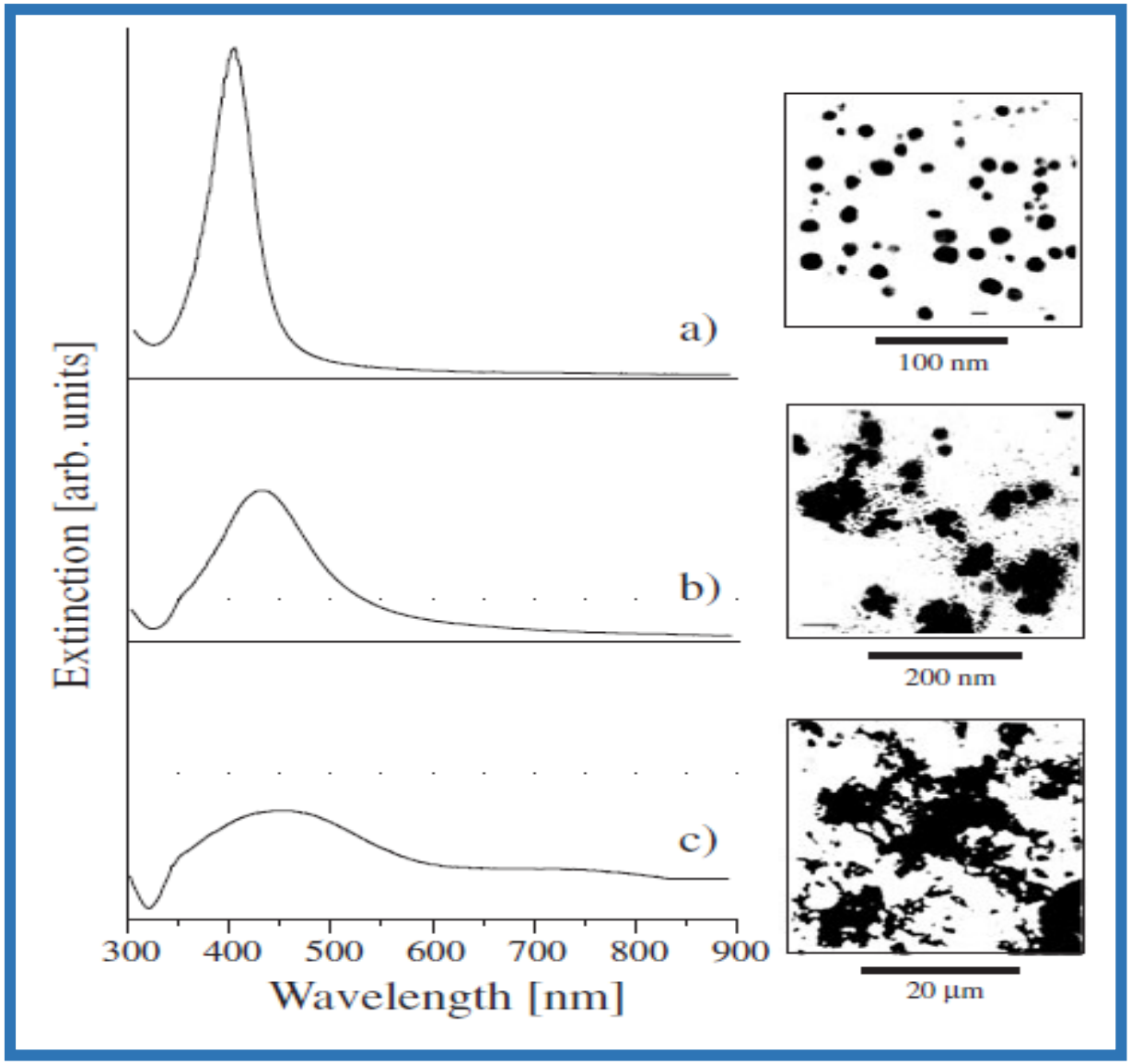

TEM Ag agregátů s n

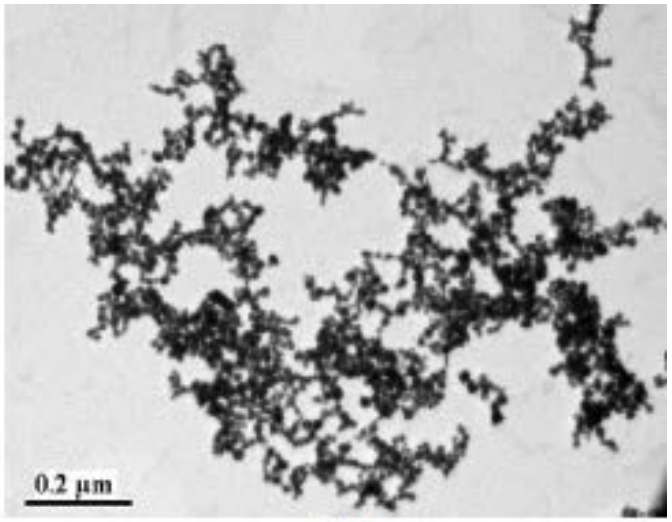

(A)

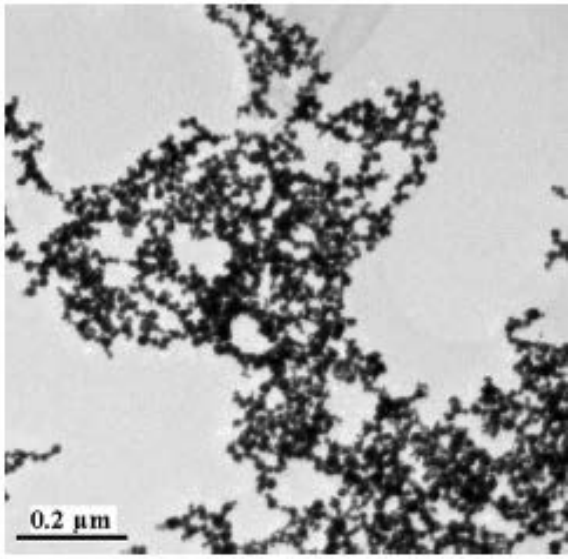

(B)

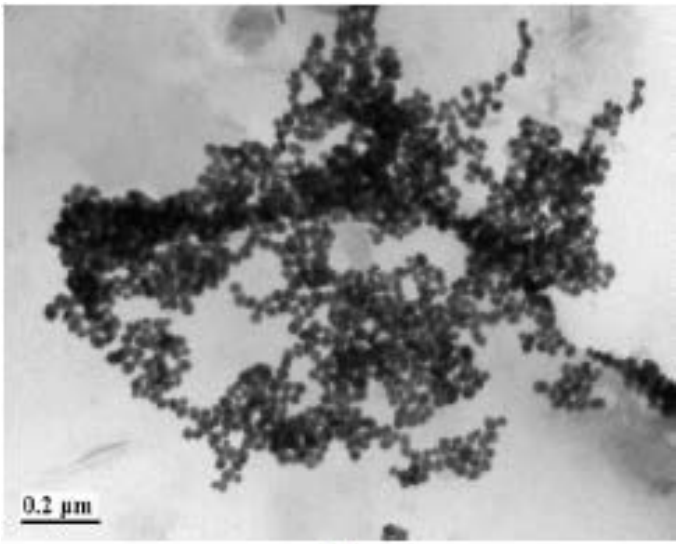

(C)

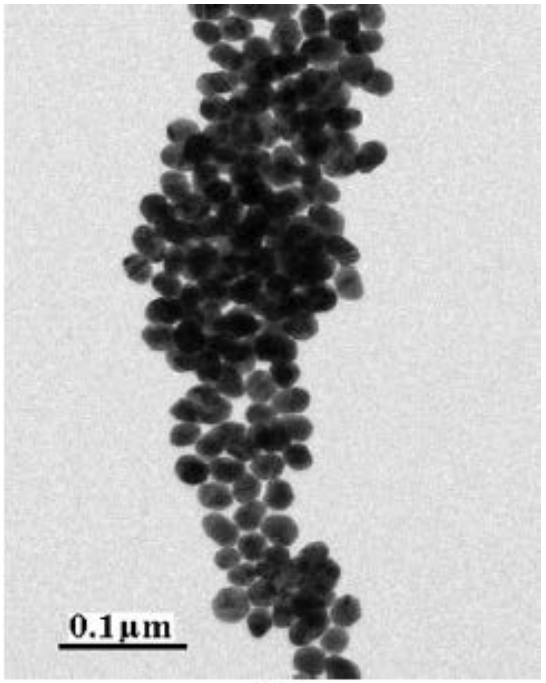

(D)

TEM images of silver aggregates with (A) cytosine, (B) guanine, (C) adenine, and (D) thymine.

Normalizovaná SERS spektra nukleobasí

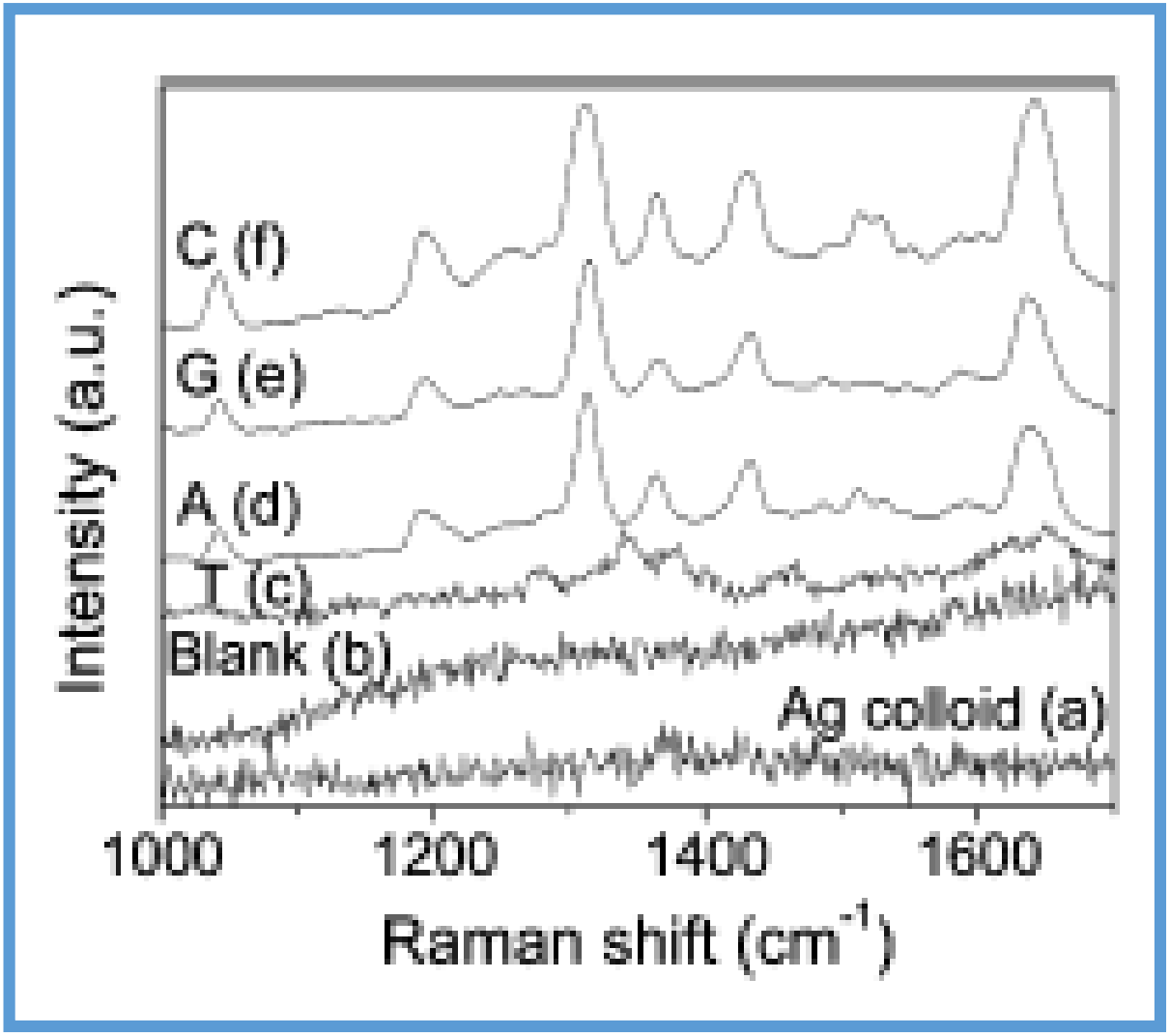

SERS spektra neurotransmitérů

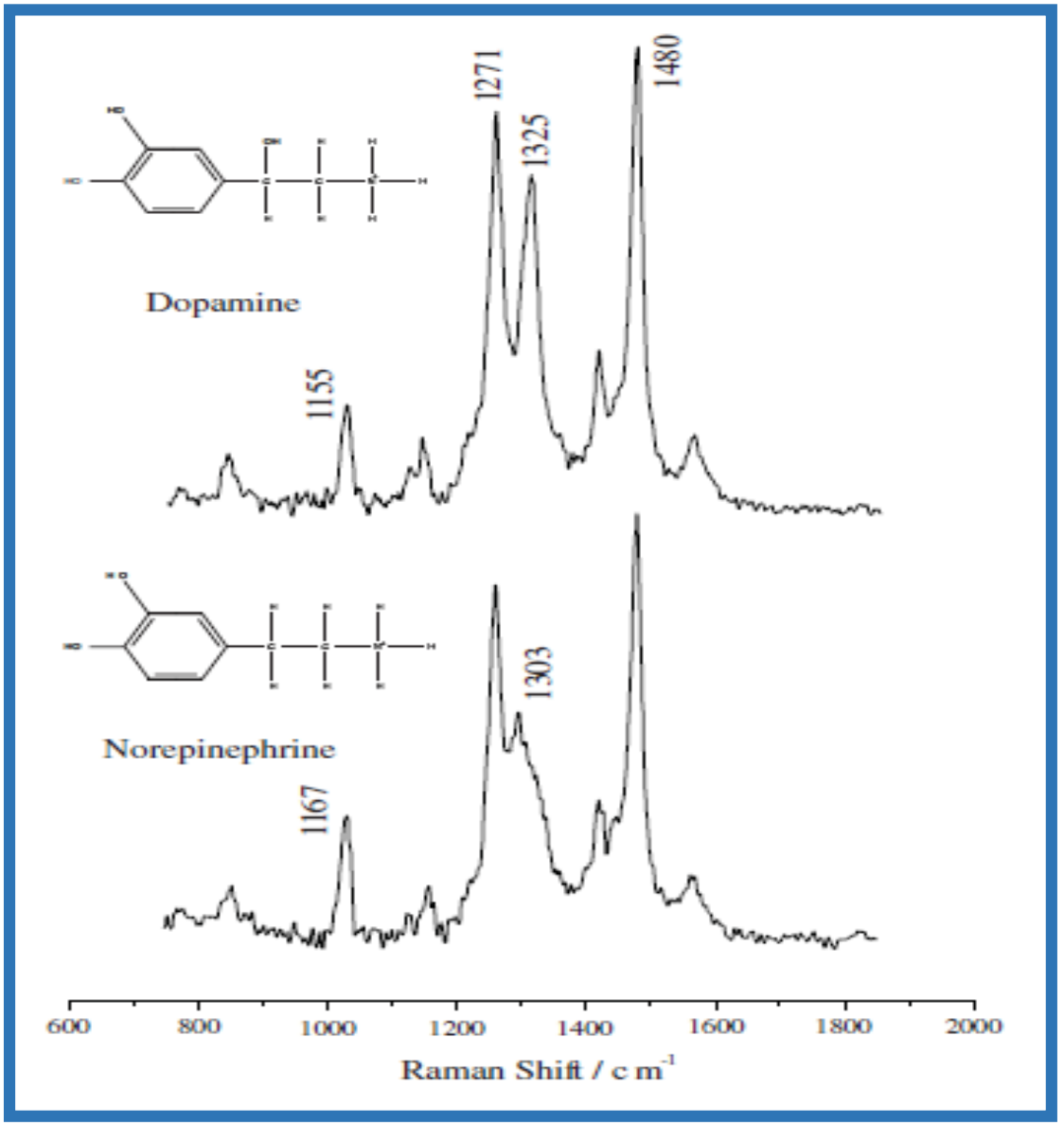

Srovnání RS a SERS spekter krátkých oligonukleotidů

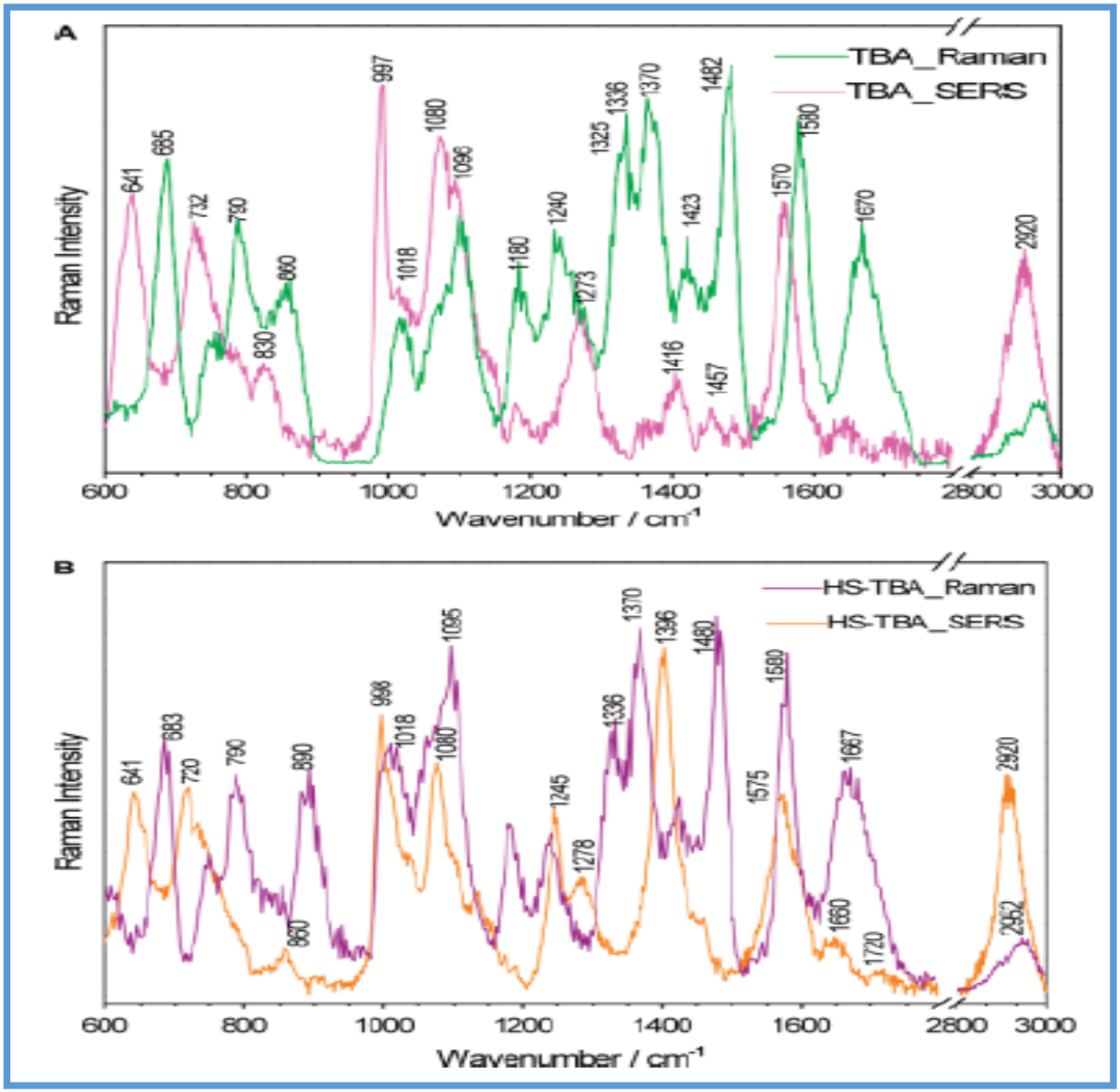

SERS a RS spektra kratkých oligopeptidů

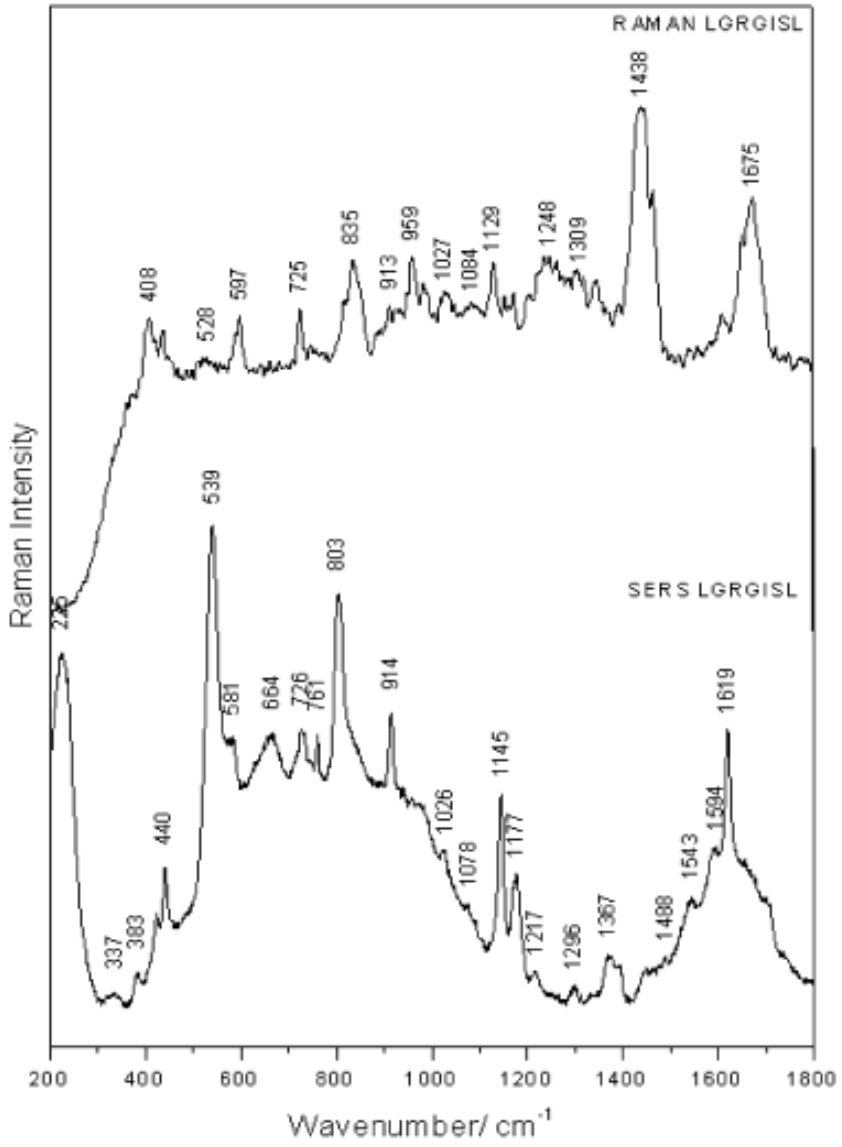

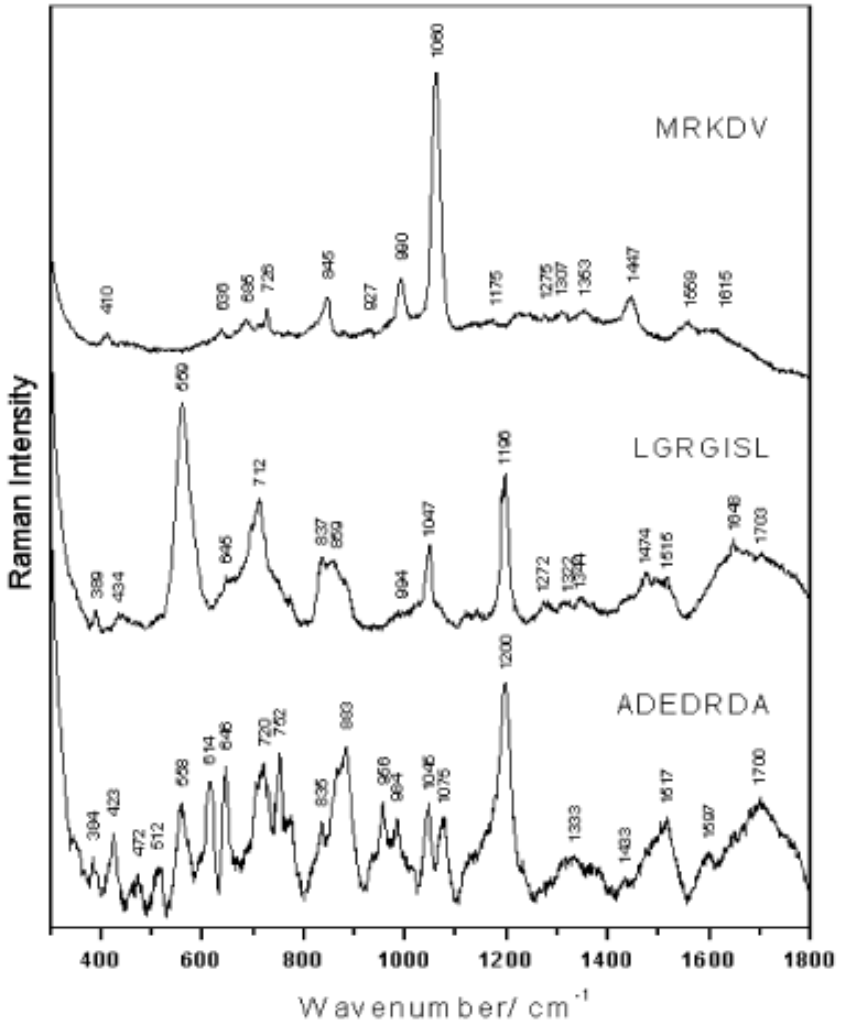

Figure 4. SERS spectra of oligopeptides MRKDV, LGRGISL and ADEDRDA. Laser line 633 nm.

Tautomerní formy 9-aminoakridinu

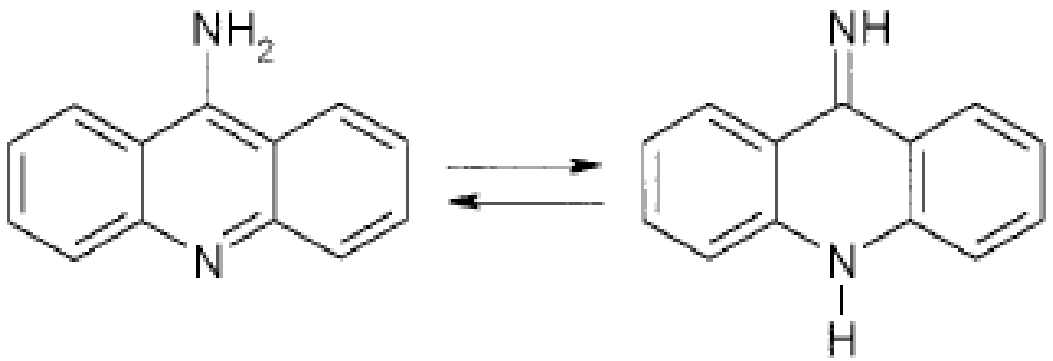

amino form imino form

Figure 1. The amino–imino tautomeric equilibrium in 9AA.

SERS spektra 9-aminoakridinu a jeho komplexu s DNA

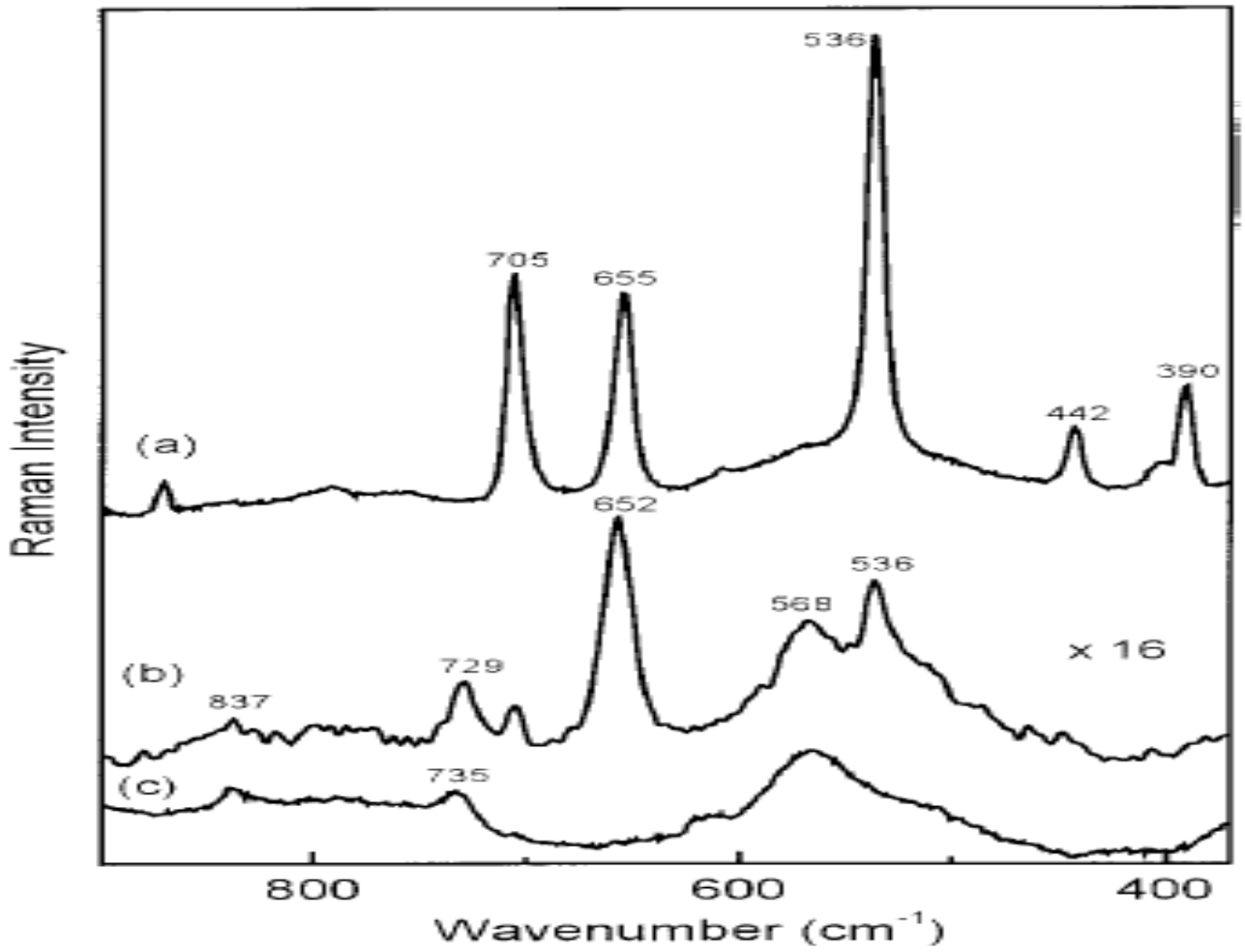

Figure 7. The SERS spectra in the 900–350 cm^{-1} region of 9AA (1.75×10^{-6} *M*; spectrum a), 9AA/DNA complex (1.75×10^{-6} *M*:0.05 mg/mL; spectrum b), and DNA, (0.05 mg/mL; spectrum c). The excitation was at 782 nm.

Schéma detekce DNA hybridizace pomoci SERS aktivní značky

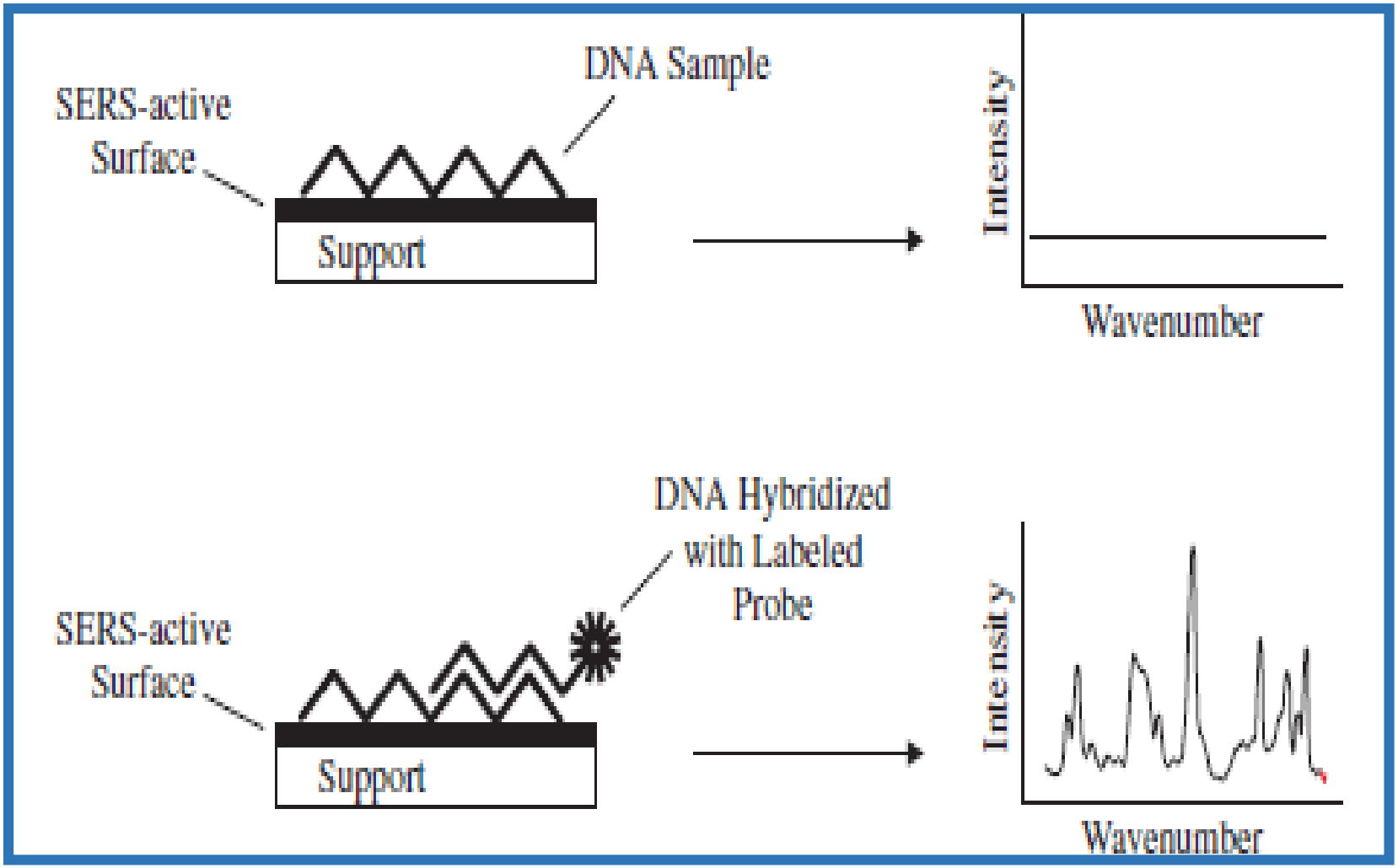

Idea přímého sekvenování DNA s využitím charakteristick
spekter bazí DNA

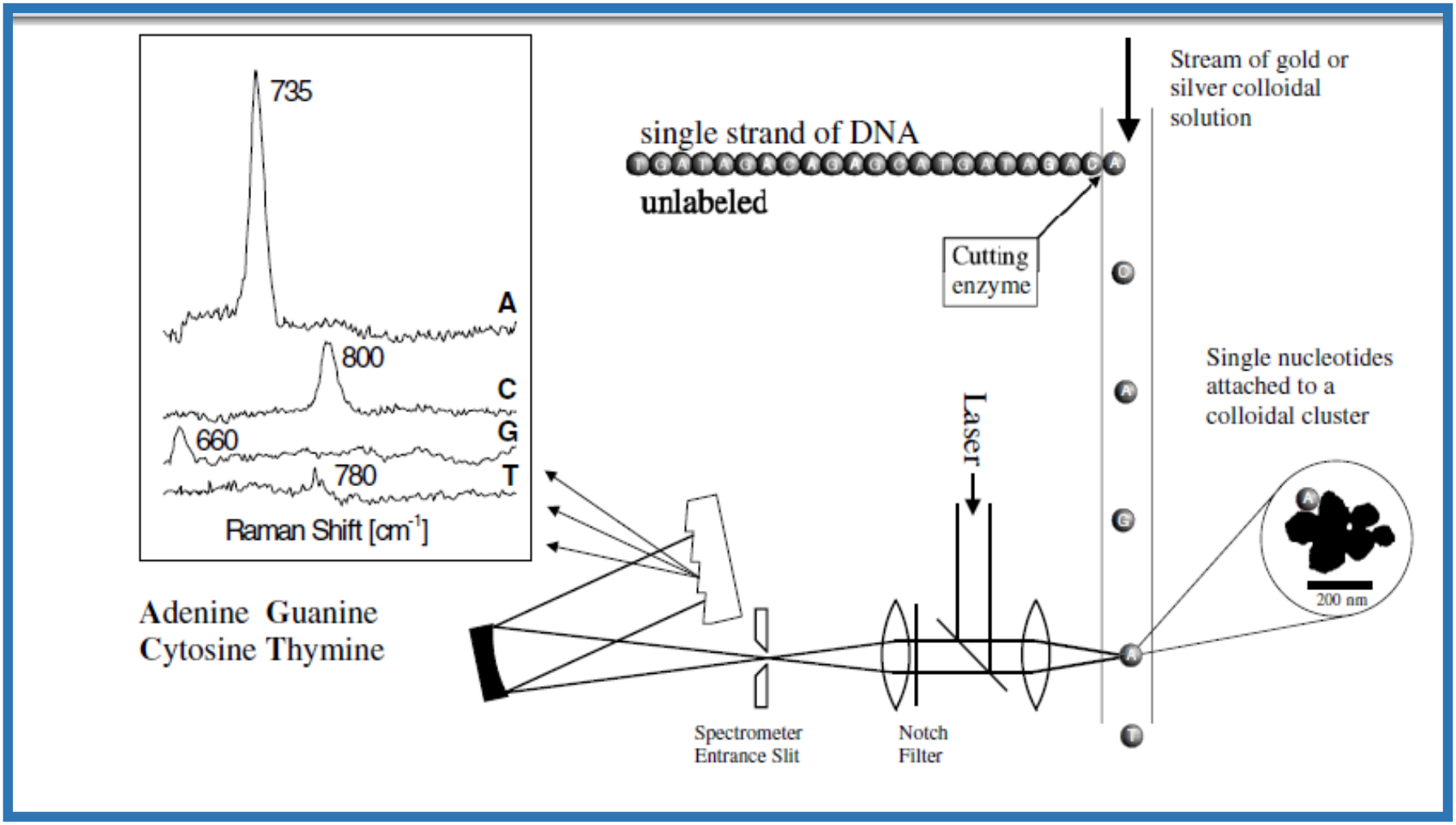

Escherichia coli, (a) elektron mikroskopický obrázek, (b) SERS spektrum buněk pokrytých Ag koloidem

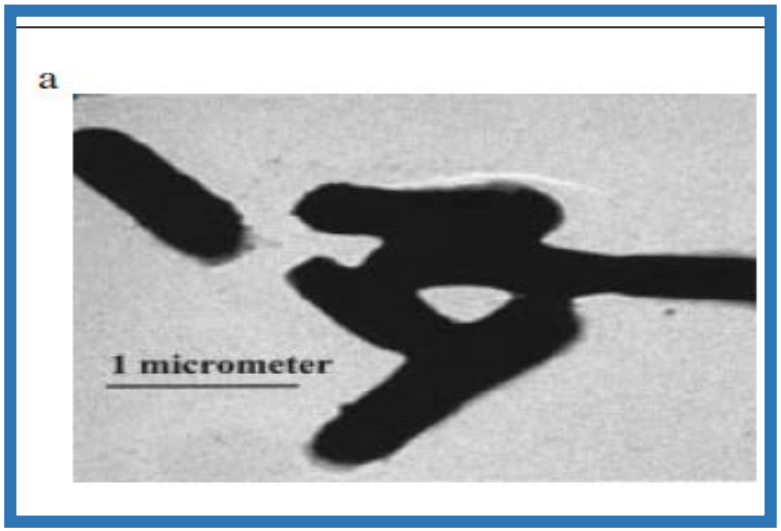

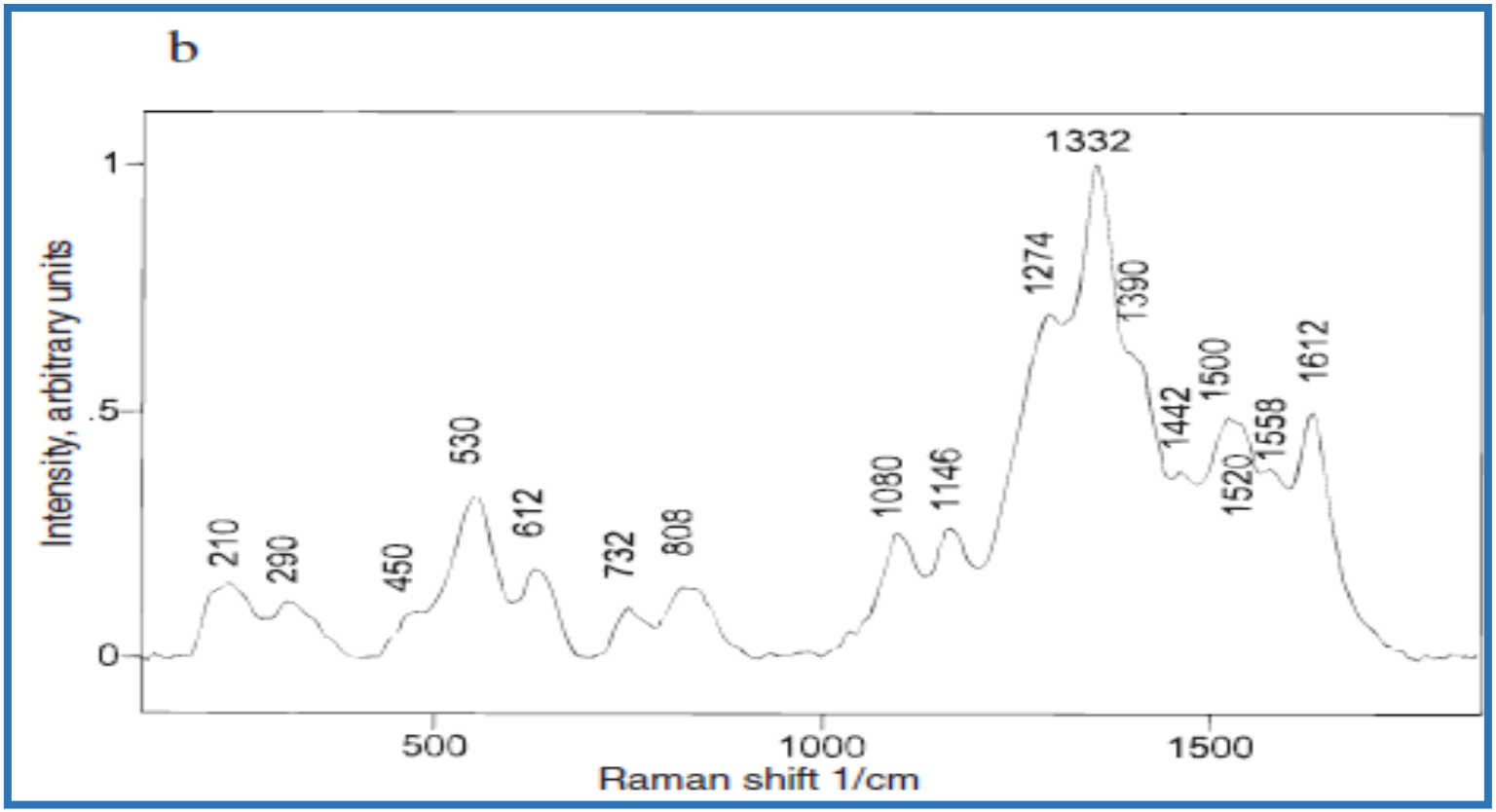

SERS spektra živých bu

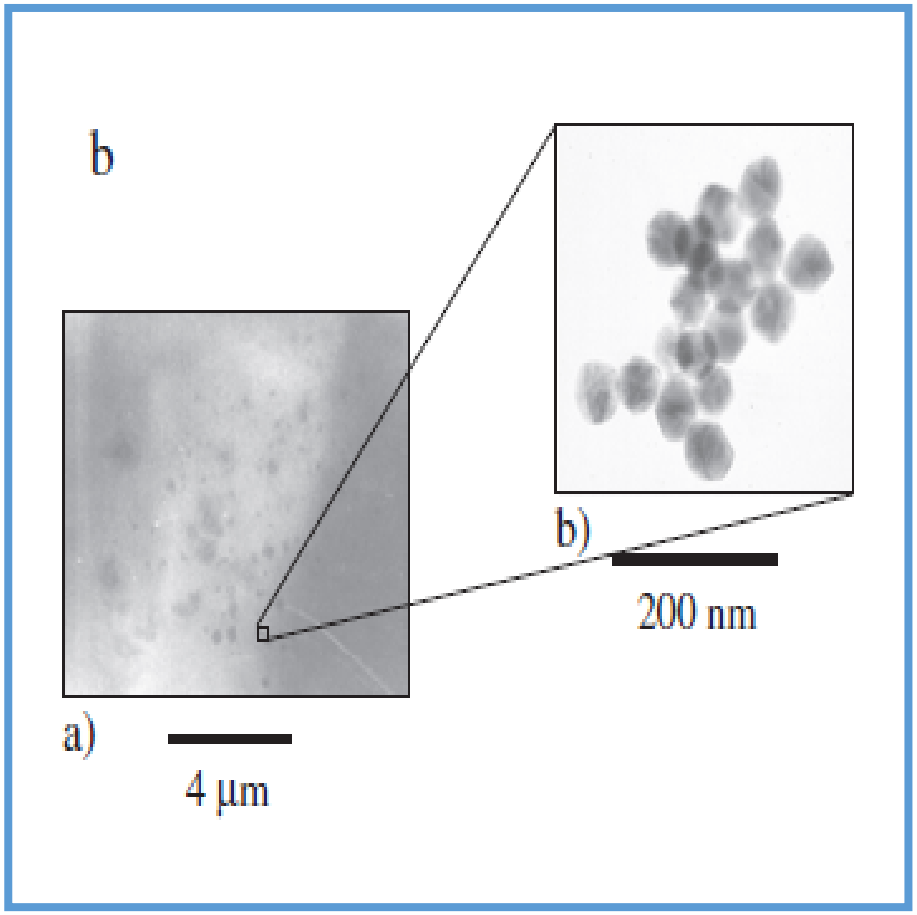

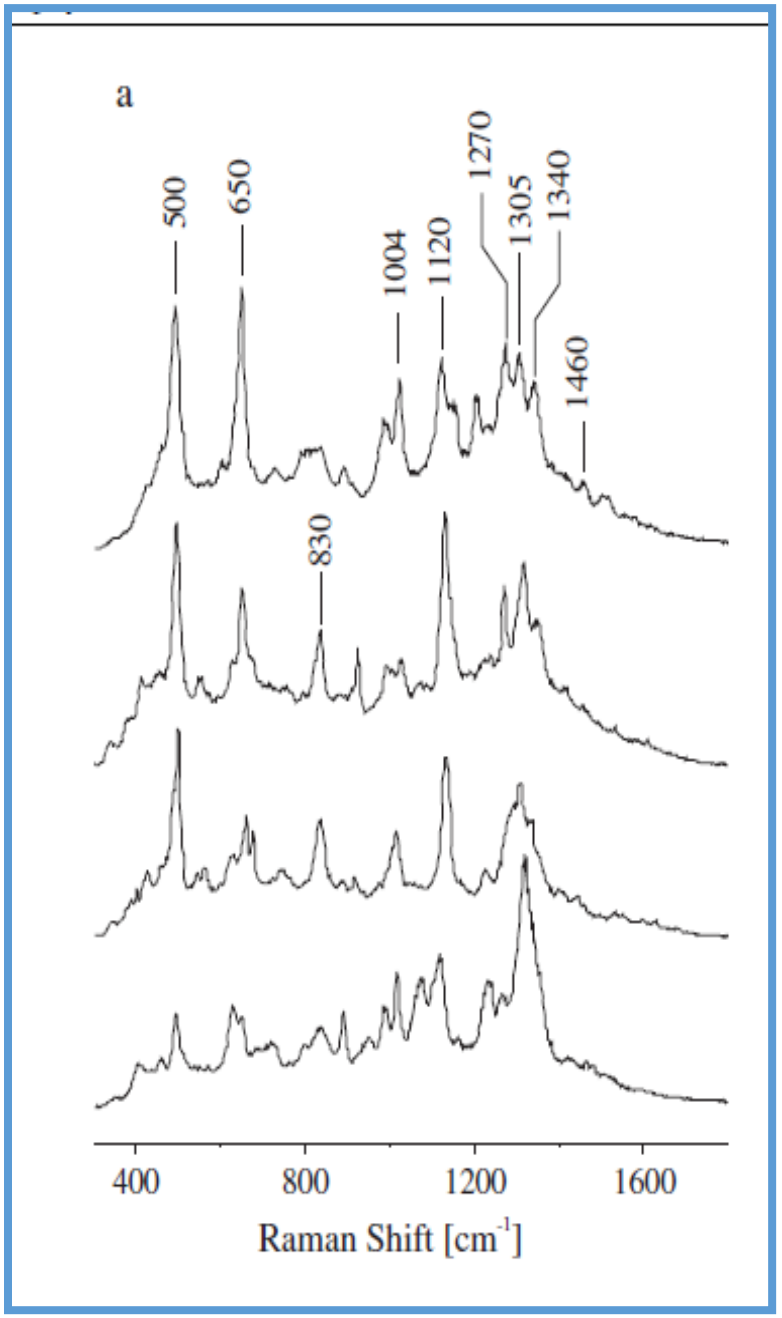

SERS spektra imobilizovaného flavinu v závislost na potenciálu

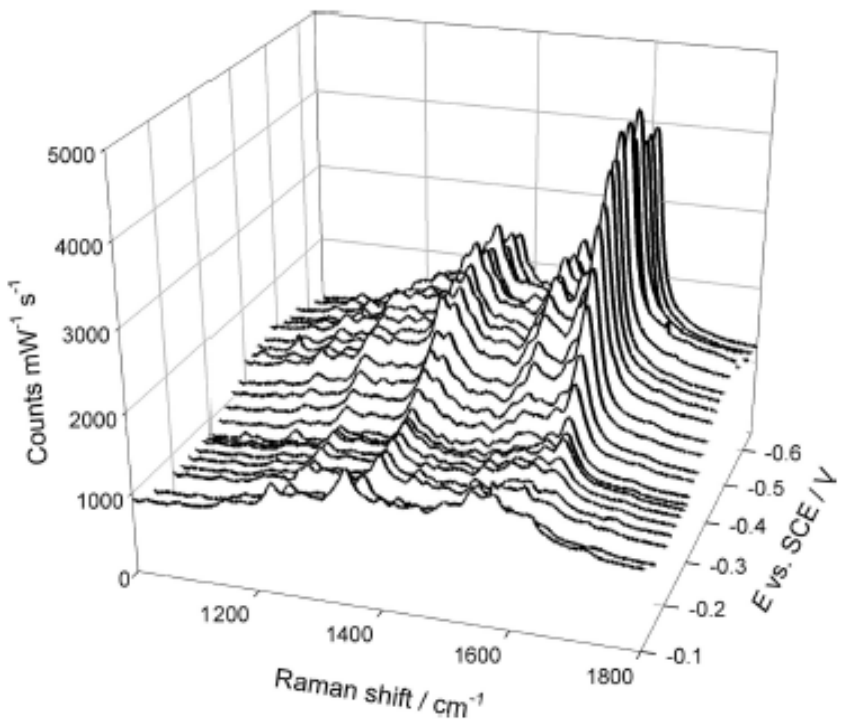

Figure 5. In situ electrochemical SER spectra for flavin immobilized on an SSV silver film produced using template spheres of 900 nm diameter and 540 nm thickness with a He−Ne laser (633 nm, single 10 s accumulation, 3 mW laser power, recorded in Tris buffer, pH 7). The sample was purged with N_2 for 20 min at the beginning of the experiment and then for 1 min between each measurement.

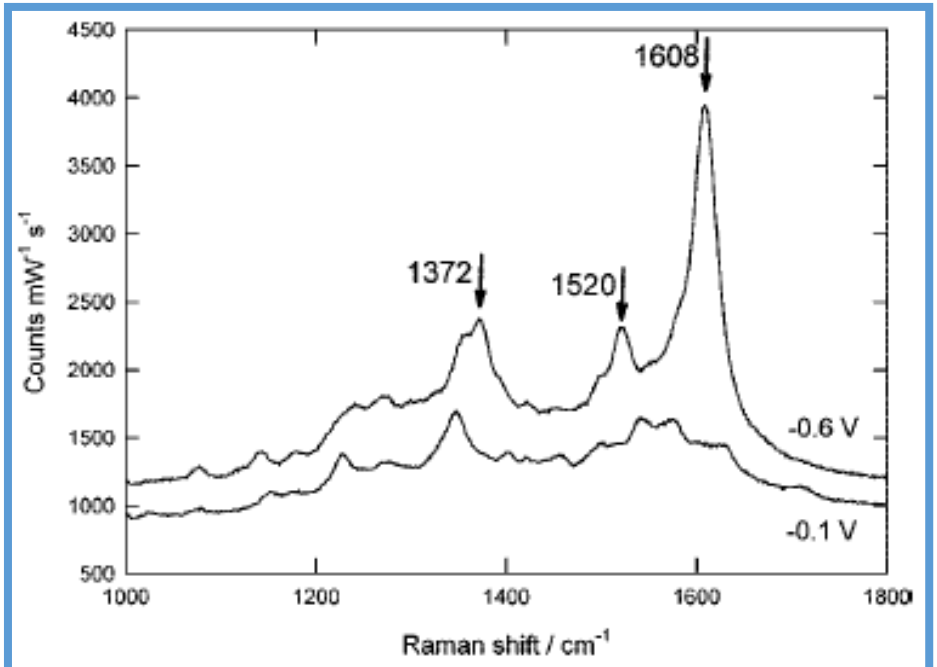

Figure 6. SER spectra of immobilized flavin recorded at −0.1 and −0.6 V vs SCE.